THERMAL AND MAGNETIC EVOLUTION OF A CRYSTALLIZING BASAL MAGMA OCEAN IN EARTH'S MANTLE

A PREPRINT

Nicolas A. Blanc
Institute for Geophysics and Planetary Physics, Scripps Institution of Oceanography
University of California San Diego
La Jolla, California, USA
nblanc@ucsd.edu

Dave R. Stegman
Institute for Geophysics and Planetary Physics, Scripps Institution of Oceanography
University of California San Diego
La Jolla, California, USA

Leah B. Ziegler
Institute for Geophysics and Planetary Physics, Scripps Institution of Oceanography
University of California San Diego
La Jolla, California, USA

September 30, 2019

ABSTRACT

We present the thermochemical evolution of a downward crystallizing BMO overlying the liquid outer core and probe its capability to dissipate enough power to generate and sustain an early dynamo. A total of 61 out of 112 scenarios for a BMO with imposed, present-day Q_{BMO} values of 15, 18, and 21 TW and Q_r values of 4, 8, and 12 TW fully crystallized during the age of the Earth. Most of these models are energetically capable of inducing magnetic activity for the first 1.5 Gyrs, at least, with durations extending to 2.5 Gyrs; with final CMB temperatures of 4400 $\pm$ 500 K –well within current best estimates for inferred temperatures. None of the models with Q_{BMO} = 12 TW achieved a fully crystallized state, which may reflect a lower bound on the present-day heat flux across the CMB. BMO-powered dynamos exhibit strong dependence on the partition coefficient of iron into the liquid layer and its associated melting-point depression for a lower mantle composition at near-CMB conditions –parameters which are poorly constrained to date. Nonetheless, we show that a crystallizing BMO is a plausible mechanism to sustain an early magnetic field.

***K*eywords** Basal magma ocean dynamo · Early Earth dynamo · Molten silicates

1 Introduction

A fundamental constraint on the thermal evolution of the Earth is that of the presence of a magnetic field since at least 3.45 Ga [1], and possibly even since 4.2 Ga [2]. Some recent estimates on the thermal conductivity of the Earth's core imply estimates of core heat flow on the order of 15 TW [3, 4, 5] which favors a young (<500 Myr) inner core [6, 7, 8, 9]. Since the buoyancy sources associated with inner core nucleation (light element concentration and latent heat) are the main sources of power dissipation for magnetic activity generation for the current field [10, 11], generating a geodynamo in the absence of an inner core (through secular cooling of the core) poses significant challenges [6]. Moreover, thermal evolution models that incorporate high core heat flow, such as those implied by higher thermal conductivity values, also imply extensive melting of the mantle (i.e. a "thermal catastrophe") [12, 13, 14].

Sustaining a dynamo for >3 Gyrs in the absence of an inner core led to the proposal of alternative mechanisms for powering a geodynamo, such as the exsolution of light material across the core mantle boundary (CMB) [15, 16, 17, 18]. Experimental determination of exsolution reactions [17, 18, 19] indicate this may be a viable mechanism, however, there are still questions as to whether either would provide sufficient power, duration, or be active during the period of interest [20, 21, 19].

Exsolution mechanisms explicitly occur across a metal-silicate interface that is liquid on both sides [17, 19], thus invoking a long-lived basal magma ocean (BMO) atop the core [22, 23] which would initiate at mid-mantle depths and crystallize downwards to the core. A giant impact as large as one suggested to lead to the formation of the Moon may have been energetic enough that Earth's initial condition was completely molten [24, 25, 26], however the initial depth of an emergent BMO is subject to uncertainty in the equation of state of lower mantle composition, its melting curve, the adiabatic gradient as determined by its material properties, and the dynamics of phase separation [27, 28, 29, 30, 31, 32]. The scenario of whether the BMO, if electrically conductive enough, could be capable of generating a dynamo was explored as a potential mechanism for providing a magnetic field during the early Earth [33]. Recent theoretical calculations of the electrical conductivity of molten silicates at P-T conditions appropriate for the CMB report values that support it as a material that is sufficiently electrically conductive [34, 35, 36, 37, 38, 39].

The previous conceptual model for a BMO-powered dynamo [33] used an idealized phase diagram for the evolution of a crystallizing basal magma ocean [22]. In this study, we present the thermochemical evolution of a downward crystallizing BMO (see Figure 1) using recent thermodynamic and mineral physics for molten silicates at lower mantle P-T conditions [40, 29, 32], and their associated entropy budgets provide a more robust measure of evaluating the circumstances under which the BMO played a role in the magnetic evolution of early Earth. We constrain our models with the early magnetic history of Earth and estimates of the current CMB temperature.

2 Model and Methods

We build upon an established theory for gross thermodynamics of the Earth's core with a solidifying inner core [41, 42, 9] and apply it to the scenario of a downward crystalizing BMO layer overlying Earth's core. We adapt an existing general 1D model for thermochemical evolution of the Earth's core [7] to study the evolution and fractional crystallization of an FeO-enriched basal magma ocean (see Fig. 5C, D in [32] for reference). We approximate the molten layer to be a fluid in hydrostatic equilibrium with an adiabatic temperature where a homogenously-mixed composition is maintained by vigorous convection everywhere outside thin boundary layers.

The global energy budget for the BMO-layer determines its evolution by balancing the heat flux across the top of the layer (Q_{BMO}) against the sum of all heat sources within the layer. While the energy budget contains information about the cooling rate of the layer and, inevitably, the rate at which it crystallizes, it lacks information about the dynamo as all magnetic energy is converted into heat within the layer. Dynamo information is inherently embedded in the entropy budget equations which relate all entropy sources to the two most significant entropy sinks, thermal diffusion and Ohmic dissipation; the power available to drive a dynamo is related to the latter. Combining the energy budget with the associated entropy budget provides sufficient information to describe and characterize the thermal and magnetic evolution of the BMO over time.

2.1 Energy Budget

The total energy, Q_{BMO}, extracted through the top of the BMO layer by the overlying solid mantle is the sum of all energy sources within the layer. The complete energy budget can be written as

$$Q_{BMO} = Q_s + Q_g + Q_L + Q_r + Q_P + Q_H, \tag{1}$$

which includes the secular cooling of the layer, Q_s, the gravitational potential energy released during solidification, Q_g, the latent heat generated as the layer solidifies, Q_L, the heat due to radioactive decay, Q_r, the heat due to a change in pressure due to thermal contraction, Q_P, and the heat of reaction, Q_H. The contribution from the last two terms is negligible, they are only included for completeness. Following [41, 42, 7], the first four terms except for Q_r can be related to the cooling rate, dT_r^{BMO}/dt, where T_r^{BMO} is the temperature of the layer at the solidification front radius, r. Indeed, these terms have been previously derived for the case of the solidifying inner core at length elsewhere [41, 42, 9, 7], thus we briefly summarize their analytical expressions below and, where necessary, explain the modification made in adapting these formulations to better represent the BMO scenario.

The first term in Eq. 1 describes the energy associated with the secular cooling of the layer and it can be expressed as

$$Q_s = -\int \rho\, C_p \frac{dT_r^{BMO}}{dt}\, dV, \tag{2}$$

where ρ and C_p are the density and specific heat capacity of the layer, respectively. This term is simply the amount of heat released as the layer cools volumetrically. The second term in 1 is related to the amount of gravitational energy released due to the re-distribution of lighter elements to the top of the layer, or equivalently the displacement of denser elements to the bottom of the layer, upon crystallization. It is given by

$$Q_g = \int \rho \, \psi \, \alpha_{BMO} \frac{Dc}{Dt} \, dV, \tag{3}$$

where ψ is the gravitational potential. The parameter α_{BMO} is a dimensional coefficient which specifies the sensitivity of the layer density to the enrichment of FeO, analogous to α_c described in [42] due to the presence of light elements in the core. It is given by

$$\alpha_{BMO} = -\frac{1}{\rho} \left(\frac{\partial \rho}{\partial c} \right)_{P,T} \approx \frac{\Delta \rho_{BMO}}{\rho_r^{BMO} \Delta c_{FeO}^l}, \tag{4}$$

where ρ_r^{BMO} is the density of the BMO layer at the solid-liquid interface radius r, and $\Delta \rho_{BMO}$ is the density jump across the interface due to the change in concentration of the liquid, Δc_{FeO}^l, as it becomes progressively enriched in FeO upon solidification.

The change in concentration dependents on the rate at which FeO is incorporated into the solidifying bridgmanite phase which is controlled entirely by the partitioning coefficient, D_{FeO}. This allows for the following expression, $\Delta c_{FeO}^l = c_{FeO}^l (1 - D_{FeO})$ which relates the amount of FeO in the liquid, c_{FeO}^l, to its partitioning coefficient. We estimate values for α_{BMO} (see Table 2) using $\Delta \rho_{BMO} = 200 - 300$ kg/m^3 from [32] and two different partition coefficients for FeO: $D_{FeO} = 0.1$ [43] and $D_{FeO} = 0.5$ [44].

Lastly, the amount of gravitational energy released at the interface depends on the rate at which lighter elements are re-distributed to the top of the layer, Dc/Dt. Following [42], we relate this term to the rate at which the interface crystallizes,

$$\frac{Dc}{Dt} = Cc \, \frac{dr_{top}}{dt} = \frac{4\pi \, r_{top}^2 \, \rho_{top} \Delta c}{M_r^{BMO}}, \tag{5}$$

where r_{top} and ρ_{top} are the radius and the density at the top of the BMO layer, Δc is the change in concentration of the liquid layer, and M_r^{BMO} is the mass of the liquid layer.

The third term in 1 accounts for the latent heat generated and released at the interface as the layer solidifies and it depends on the rate at which this process occurs:

$$Q_L = 4\pi \, r_{top}^2 L_H \, \rho_{top} \frac{dr_{top}}{dt}, \tag{6}$$

where L_H is the latent heat of reaction which is assumed to be constant. The last term in 1 is simply the heat generated within the volume of the BMO layer by the decay of radioactive elements. Considering a density ρ and a volumetric heating rate, h, over a volume, V, this term can be written as

$$Q_r = \int \rho h \, dV. \tag{7}$$

The heat production is time-dependent according to the assumed BSE concentrations, long-lived radioactive decay energies and halflives, which are given in Table 1. Making use of the formulations presented above, the total energy budget 1 for a crystallizing BMO layer can be expressed as follows

$$\begin{aligned} Q_{BMO} &= -\int \rho \, C_p \frac{dT_r^{BMO}}{dt} \, dV + \int \rho \, \psi \, \alpha_{BMO} \frac{Dc}{Dt} \, dV \\ &\quad + 4\pi \, r_{top}^2 L_H \, \rho_{top} \frac{dr_{top}}{dt} + \int \rho h \, dV \\ &= Q_s + Q_g + Q_L + Q_r. \end{aligned} \tag{8}$$

2.2 BMO solidification model

In this work, we consider a BMO layer overlying the liquid core crystallizing from the top down towards the CMB, whose thickness is determined by the intersection of the adiabat and the melting curve as shown schematically in Figure 1. As the layer cools, the adiabat intersects the melting curve at greater depths causing the layer to shrink. The initial thickness of the layer is determined by the initial temperature; here, we define two different values for the initial temperature of the layer resulting in two initial thicknesses: $r_0^{top} = 4242$ km and $r_0^{top} = 4458$ km.

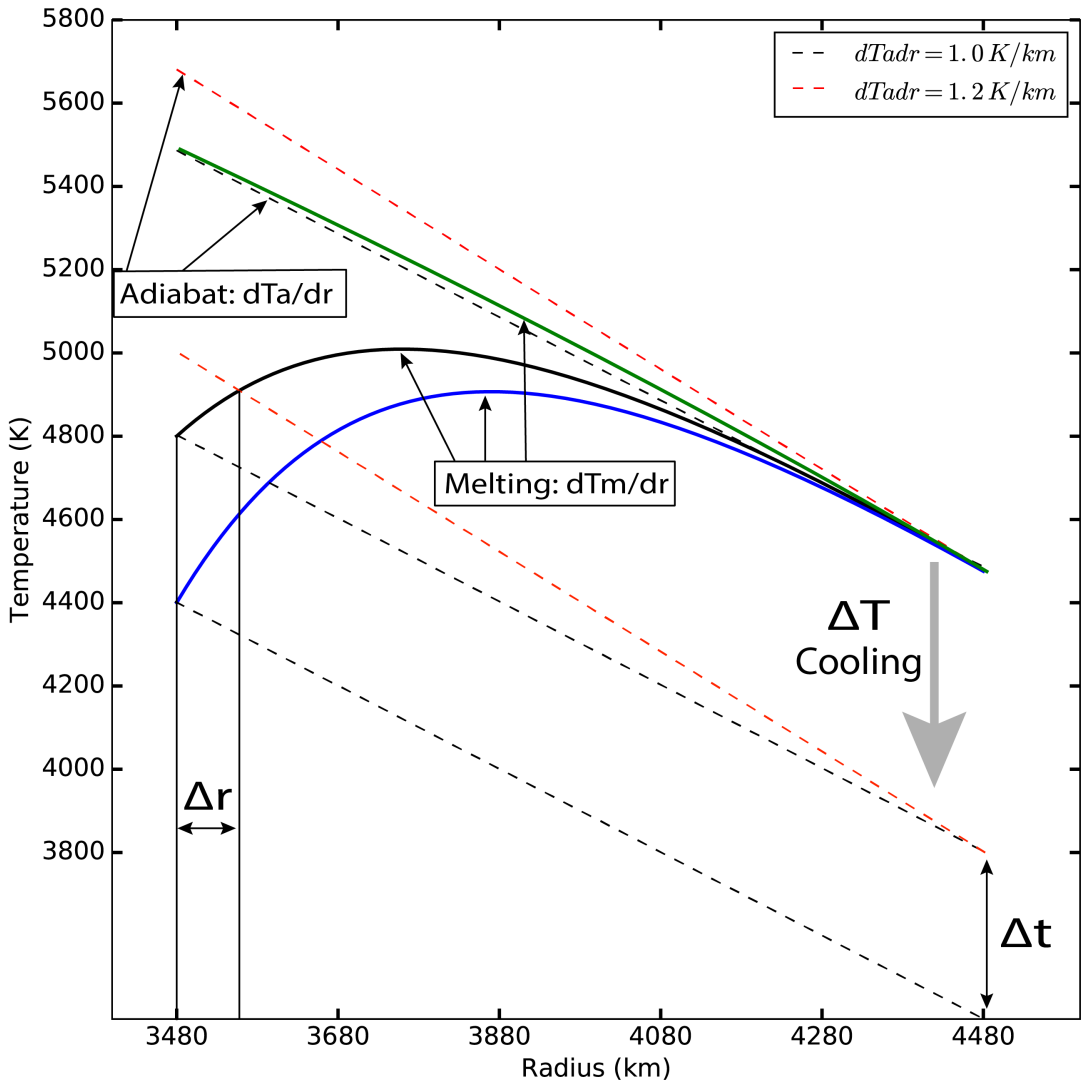

Figure 1: BMO thermal evolution diagram. The thickness of the BMO layer is defined by the intersection of the adiabat, T_a, and the melting curve, T_m. The corresponding temperature at the CMB is determined by tracking the adiabat to the appropriate radius. Secular cooling of the layer over time moves the adiabat to lower temperatures, intersecting the melting curve at greater depths thus crystallizing the layer downward toward the CMB. Imposing a larger melting point depression at the CMB to the melting curve (black versus blue solid curves) prolongs the life of the BMO layer as it is required to cool an additional amount of time, Δt, to fully crystallize. Moreover, at a time, t, two different adiabats (red and black dashed lines) will intersect a given melting curve at different points changing the thickness of the BMO layer at that point in time by an amount Δr.

Table 1: Input parameters.

Definition	Symbol	Units	Value	Reference
Density	ρ	Kg m^{-3}		[46]
Density jump	$\Delta\rho_{BMO}$	Kg m^{-3}	200 - 300	[32]
CMB pressure		GPa	135	
Mantle specific heat	$C_{p_{mantle}}$	J Kg^{-1} K^{-1}	1000	[22]
Core specific heat	$C_{p_{core}}$	J Kg^{-1} K^{-1}	860	[22]
Mass of Core	M_{core}	Kg	2×10^{24}	[22]
Adiabatic gradient	dT_a/dr	K / km	1.0/1.2	
Entropy of melting per unit mass	Δs	J Kg^{-1} K^{-1}	300	[22]
Melting temperature at the CMB		K	5400	[45]
Melting-point depression at the CMB	T_m^0	K	700 / 1000	
Thermal conductivity of the mantle	k	W m^{-1} K^{-1}	8	[22]
Initial FeO concentration		wt%	15.99	[32]
FeO partition coefficient	D_{FeO}		0.1 / 0.5	[43, 44]

We implement a lower mantle adiabat with two different gradients, and utilize the melting curve for a peridotite mantle composition [45, 40]. Two different melting point depressions at the CMB, $T_m^0 = 700$ K and $T_m^0 = 1100$ K are imposed onto the undepressed melting curve (green curve in Figure 1) to represent the depression induced by the progressive enrichment of the liquid layer in FeO as it crystallizes. The density of the layer is estimated to be similar to that of the current lower mantle for which we utilize a polynomial fit to the Preliminary reference Earth model (PREM) [46].

We take the initial concentration of FeO in the liquid to be that of [32] for a pyrolitic melt after 50% crystallization of bridgmanite and allow it to evolve using two different (end-member) values for the partition coefficient: $D_{FeO} = 0.5$ [44], and $D_{FeO} = 0.1$ [43]. However, since the behavior of D_{FeO} has only been characterized for Fe partitioning between bridgmanite and liquid compositions which have relatively modest Fe concentrations, we would expect D_{FeO} to deviate from these measured values once the system has evolved to be heavily Fe enriched. Accordingly, we adopt a conservative threshold at $c^l_{FeO} = 50\, wt\%$ for the interpretation of our model results once the concentration of FeO in the liquid exceeds $50\, wt\%$, as we anticipate the partition coefficient for such a state to deviate from the constant value being applied. All input parameters are presented in Table 1.

The evolution of all models is largely controlled by the amount of heat being extracted by the solid mantle from the top of the BMO layer and the amount of radiogenic heat produced within the layer. Henceforth we refer to the combination of these two parameters as "cooling history". The internal heating of the mantle corresponds to a Bulk Silicate Earth (BSE) model [47] comprises of the decay energies for the 4 long lived radioactive isotopes (U235, U238, Th232, and K40) in the appropriate ratios. The radiogenic heat production over time is prescribed by the sum of the abundance and decay energies for the 4 isotopes and their corresponding half-lives, based upon the present day heat production for the BSE of 20 TW. Approximately 8 TW of the total BSE complement is assumed to reside in the continental crust, and the remaining 12 TW (out of the 20 TW total) therefore resides within the mantle, for which we consider 3 scenarios (4, 8 or 12 TW) for how much is contained within the BMO, representing 33%, 67%, or 100% of the available heat production shown as dashed curves in Figure 2. The complement of radiogenic heat producing elements initially in the BMO are assumed to remain in the BMO for its entire evolution, and thus for models that have completely solidified, the entirety of the radiogenic heating would be contained within a very thin layer in the mantle atop the CMB.

The cooling of the BMO, $Q_{BMO}(t)$, is controlled by a cooling history that is prescribed at the interface between solid and liquid mantle with a present-day value of 15, 18, and 21 TW shown as solid curves in Figure 2. Thus, the core heat flow across the CMB, Q_{cmb}, at the present day spans values between 9-14 TW, which is the difference between Q_{BMO} and Q_r for the cooling histories considered in Table 1. The differences between Q_{BMO} and Q_r for the various combinations also imply higher or lower secular cooling rates for the mantle, as the larger value chosen for Q_r leaves a smaller amount of the available 12 TW for heating the mantle above the BMO. For example, Q_r of 8 TW in the BMO leaves only 4 TW in the solid mantle, leading to faster secular cooling of the mantle which would presumably drive faster secular cooling of the core, and hence this value of Q_r is used in combination with larger Q_{BMO} values of 18 TW and 21 TW, corresponding to Q_{cmb} values of 10 and 13 TW, respectively.

2.3 Entropy budget

As mentioned above, the energy budget alone provides enough information to determine the thermal evolution of the BMO layer. However, in order to fully characterize its magnetic evolution and, ultimately, determine the feasibility of dynamo activity, the entropy balance equations are required. Most importantly, the entropy associated with thermal conduction down an adiabat, E_κ, and the Ohmic heating play crucial roles in determining if a dynamo is energetically favorable once all sources of entropy are considered. An equation analogous to 1 can be written for the entropy budget identifying both sources and sinks, and cases for the core have been extensively derived elsewhere [41, 42, 9]. Below, we only present their final formulations and describe any changes made in adapting them to describe our model. The

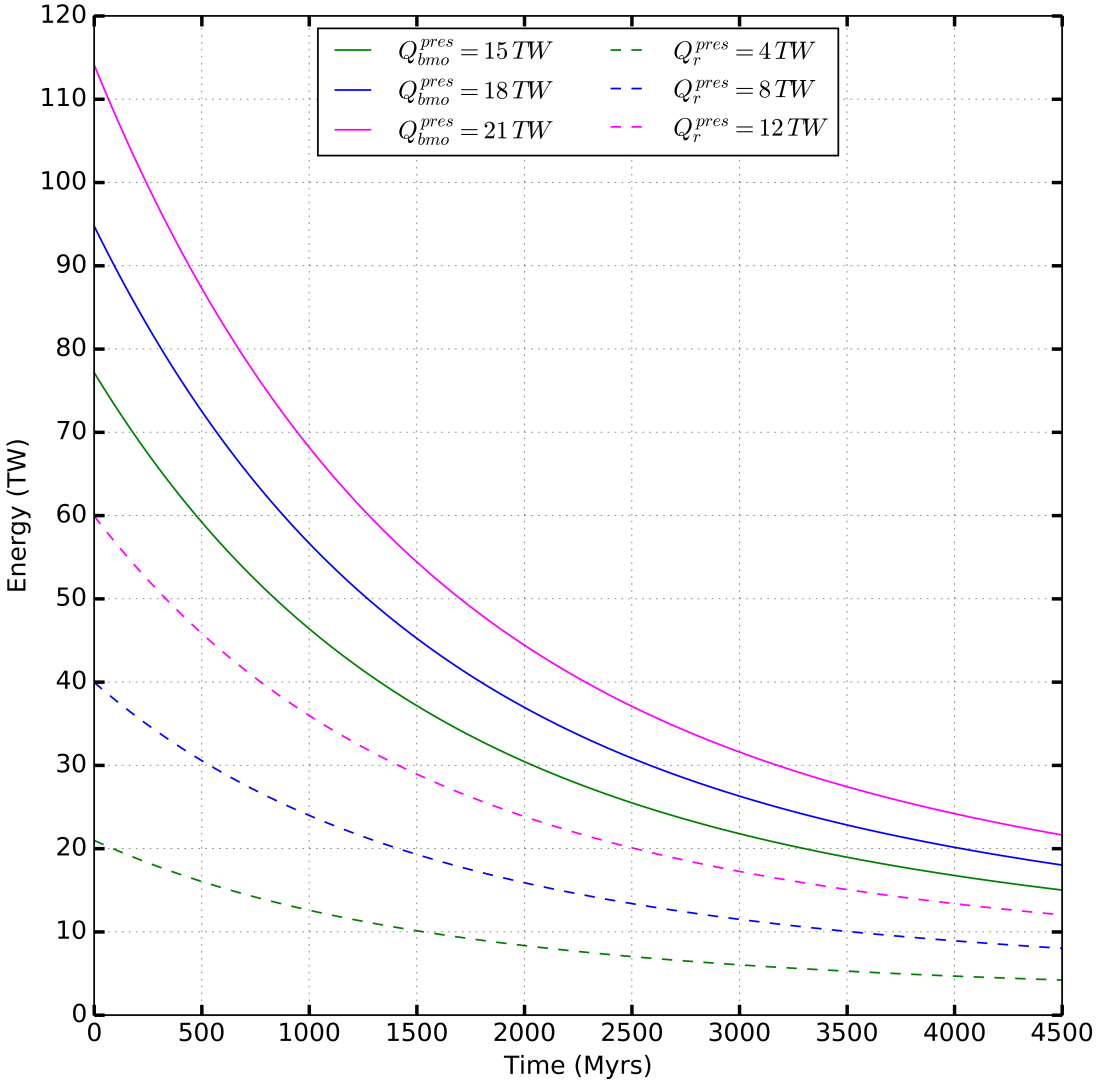

Figure 2: Cooling histories. The three different cooling histories imposed for all model runs (#1-16 in Table 2) representing 15, 18, and 21 TW present-day, adiabatic heat flux across the top of the BMO layer are shown as solid lines. Dashed lines show the three different radiogenic heating curves 4, 8, and 12 TW resulting from assuming that roughly 30%, 70%, and 100% of the BSE radioactive element budget are initially sequestered within the BMO layer.

Table 2: Model results from all the different Q_{BMO}/Q_r setups probed in this study. The input parameters for each run (1-16) within a given setup are the adiabatic gradient (dTa/dr) in K/km, the partition coefficient for FeO (D_{FeO}), compositional coefficient (α_{BMO}), and the imposed depression on the melting curve (T_m^0). Given our conservative cutoff, we report the available entropy due to Ohmic dissipation (E_Φ) at $c_{FeO}^l = 50\,wt\%$ in MW/K, and the time when this cutoff is reached (t_χ), along with the time when E_Φ falls below zero. The time it takes each model to fully crystallize (if successful) is given by t_{BMO} and the final temperature at the CMB for each case is given by T_{CMB}^{final}.

COMBO #	1	2	3	4	5	6	7	8	9	10	11	12	13	14	15	16
dTa/dr	1	1	1	1	1	1	1	1	1.2	1.2	1.2	1.2	1.2	1.2	1.2	1.2
D_{FeO}	0.1	0.1	0.1	0.1	0.5	0.5	0.5	0.5	0.1	0.1	0.1	0.1	0.5	0.5	0.5	0.5
α_{BMO}	0.3	0.3	0.4	0.4	0.4	0.4	0.3	0.3	0.3	0.3	0.4	0.4	0.4	0.4	0.3	0.3
T_m^0	700	1100	700	1100	700	1100	700	1100	700	1100	700	1100	700	1100	700	1100
Cooling history model: ★ $Q_{BMO}^{present}$ = 15 TW, Q_r = 4 TW, $Q_{CMB}^{present}$ = 11 TW																
E_Φ	280	215	351	21	1	-30	-9	-35	265	182	324	222	-40	-80	-50	-83
t_χ (Myr)	1050	1390	1070	1430	1690	2550	1670	2520	1540	1860	1600	1920	2600	3590	2560	3540
t_Φ (Myr)	2200	2810	2370	3080	1690	2210*	1620*	2120*	2920	3160	3240	3470	2250*	2560*	2140*	2450*
t_{BMO} (Myr)	2420	4070	2480	4180	2330	3930	2310	3890	4020		4180		3820		3750	
T_{CMB}^{final} (K)	4258	4310	4279	4334	4228	4279	4220	4270	4500	4433	4533	4458	4453	4401	4438	4390
Cooling history model: ■ $Q_{BMO}^{present}$ = 18 TW, Q_r = 4 TW, $Q_{CMB}^{present}$= 14 TW																
E_Φ	453	360	566	434	49	15	34	6	484	364	584	435	18	-24	7	-32
t_χ (Myr)	750	960	760	980	1160	1620	1150	1610	1060	1250	1100	1280	1690	2170	1660	2150
t_Φ (Myr)	1560	2100	1610	2250	1300	1700	1250	1640	2200	2500	2390	2700	1760	2050*	1690	1980*
t_{BMO} (Myr)	1590	2370	1630	2420	1540	2310	1530	2290	2430	3350	2510	3440	2330	3230	2300	3190
T_{CMB}^{final} (K)	3668	3684	3690	3705	3638	3654	3630	3645	3908	3864	3943	3894	3862	3823	3848	3811
Cooling history model: ◆ $Q_{BMO}^{present}$ = 18 TW, Q_r = 8 TW, $Q_{CMB}^{present}$ = 10 TW																
E_Φ	284	217	347	263	1	-31	-7	-35	267	183	322	220	-43	-81	-48	-84
t_χ (Myr)	1090	1460	1120	1490	1770	2730	1750	2700	1610	1960	1670	2020	2780	3920	2730	3850
t_Φ (Myr)	2290	2940	2470	3220	1780	2360*	1710*	2270*	3050	3330	3370	3640	2400*	2740*	2290*	2630*
t_{BMO} (Myr)	2570	4490	2640		2480	4320	2450	4270	4410				4170		4100	
T_{CMB}^{final} (K)	4342	4399	4363	4418	4312	4366	4303	4357	4583	4502	4613	4525	4536	4471	4522	4460
Cooling history model: ● $Q_{BMO}^{present}$ = 21 TW, Q_r = 8 TW, $Q_{CMB}^{present}$ = 13 TW																
E_Φ	488	390	592	464	60	25	45	15	517	398	623	470	30	-14	19	-22
t_χ (Myr)	740	950	760	970	1150	1610	1140	1600	1060	1240	1090	1270	1680	2160	1650	2140
t_Φ (Myr)	1550	2100	1600	2240	1310	1720	1270	1670	2220	2530	2390	2730	1780	2090*	1720	2030*
t_{BMO} (Myr)	1580	2360	1620	2410	1540	2300	1520	2280	2420	3340	2500	3430	2320	3220	2290	3180
T_{CMB}^{final} (K)	3671	3686	3693	3707	3642	3657	3633	3648	3911	3866	3946	3896	3865	3825	3851	3812
Cooling history model: ▲ $Q_{BMO}^{present}$ = 21 TW, Q_r = 12 TW, $Q_{CMB}^{present}$ = 9 TW																
E_Φ	303	234	365	275	5	-28	-2	-32	280	196	332	230	-39	-79	-45	-81
t_χ (Myr)	1100	1480	1130	1520	1810	2820	1790	2790	1650	2010	1710	2070	2870	4090	2820	4020
t_Φ (Myr)	2340	3040	2530	3310	1850	2480*	1780*	2400*	3150	3470	3470	3780	2510*	2900*	2410*	2800*
t_{BMO} (Myr)	2640		2720		2550		2520	4480					4360		4290	
T_{CMB}^{final} (K)	4379	4432	4401	4452	4350	4404	4342	4396	4617	4533	4644	4556	4575	4503	4561	4492

* represents the last instance in time when $E_\Phi > 0$.

entropy budget is as follows

$$E_s + E_g + E_r + E_L + E_P + E_H = E_k + E_\Phi, \tag{9}$$

where E_s, E_g, E_r, E_L, E_P, and E_H are the sources and E_k, E_Φ are the sinks; k is the thermal conductivity of the layer, and Φ represents the combined viscous and Ohmic dissipation, though the former is assumed to be negligible [9]. The small contributions from E_P and E_H are also ignored in this work. Excluding these terms, the analytical expression for the entropy budget is as the following

$$\begin{aligned} &-\int \rho\, C_p \left(\frac{1}{T_c} - \frac{1}{T}\right) \frac{dT_r^{BMO}}{dt}\, dV + \frac{Q_g}{T} + \int \rho h \left(\frac{1}{T_c} - \frac{1}{T}\right) dV \\ &- \frac{4\pi r_i^2 L_H (T_i - T_c)}{(dTm/dP - dT/dP) T_c^2 g} \frac{dT_r^{BMO}}{dt} = \int k \left(\frac{\nabla T}{T}\right)^2 dV + \int \frac{\Phi}{T}\, dV, \end{aligned}$$

which is comparable to 8 except for the Carnot efficiency term, $(1/T_c - 1/T)$.

The criteria of $E_\Phi > 0$ is commonly used for determining whether the model can generate a dynamo subject to the same assumptions that govern the applicability of this approach to core dynamics [42, 9, 10, 48], that the fluid is electrically conductive, rapidly rotating, and undergoing vigorous convection to remain adiabatic and homogenous, all of which are also appropriate for the scenario of a basal magma ocean. This framework is easily adaptable to determining the Ohmic dissipation within a BMO layer. The expression for the first three terms remain the same but the integration bounds

must be adapted to encompass the evolving thickness of the BMO layer. However, the term for entropy production due to the release of latent heat at the interface, E_L, which depends on the cooling rate of the layer and the difference between the slopes of the adiabat and the melting curve, is different to the analogous core case.

For the case of the inner core growing outward, the adiabat and the melting curve are anchored at two distinct temperatures; the CMB temperature for the adiabat and the interface (inner-core boundary (ICB)) temperature for the liquidus. However, for the BMO layer crystallizing downward towards the CMB, both the adiabat and melting curve are anchored at the same point. This results in $(T_i - T_c)$ in E_L to be zero. Another way to think about this is to consider where the latent heat is being generated. In the case of the core, latent heat is released at the ICB which drives convective motions throughout the liquid outer core directly above; but for a BMO layer, the latent heat is generated at the top of the liquid layer, so it does not contribute to convection in the liquid below. Finally, it is clear from these equations that aside from requiring entropy sources to be sufficiently energetic to power the dynamo, E_k cannot be too large (i.e. large values of k) as this would result in most of the entropy being conducted away along the adiabat and not be available to power a dynamo.

3 Results

A total of 112 models were simulated, but only 61 models fully crystallized their BMO layer during the age of the Earth. The input parameters for all model runs and their diagnostic outputs are provided (see Table 1 and 2, respectively). The final CMB temperature for all models that fully crystallized during the age of the Earth falls within the plausible range for present-day best-estimate for inferred temperatures at the CMB [49] as shown in Figure 3.

The longevity of the BMO layer varies greatly between models, ranging from short-lived layers crystallizing in 1.5 Gyrs to long-lived layers taking as much as 4.5 Gyrs to fully crystallize. The dominant parameters controlling the thermal evolution of the BMO layer are the imposed depression on the melting curve and the adiabatic gradient; these effects are shown schematically by arrows in Figure 3. For a given cooling history, imposing a larger melting-point depression extends the life of the BMO layer but it has a negligible effect on the final CMB temperature. However, introducing a steeper adiabatic gradient ($dTa/dr = 1$ K/km for filled marker vs $dTa/dr = 1.2$ K/km for unfilled markers in Figure 3) not only extends the time it takes the BMO layer to fully crystallize, but it also results in a hotter present-day CMB temperature. Changing both parameters simultaneously appears to have an almost linear additive effect.

The general trend observed in Figure 3 is primarily controlled by the total heat budget available to drive the BMO evolution, as defined by the particular cooling history imposed (i.e. combination of $Q_{BMO}^{present}$ and Q_r from Figure 2). Indeed, the fastest cooling models, those on the bottom left, have a bigger heat budget than the slower cooling models on the top right. Moreover, our choice of curves for Q_{BMO} and Q_r and their inherent curvatures causes the effects due to melting-point depression and adiabatic gradient to be more pronounced on the slower cooling models, with some of these taking as much as 4.5 Gyrs to fully crystallize. A batch of 32 models with Q_{BMO} = 12 TW and Q_r = 4 and 8 TW (corresponding to Q_{CMB} = 8 and 4 TW, respectively) were probed and none successfully crystallized the entirety of their BMO layer during the 4.5 Gyrs time window. Indeed, 19 other models with the cooling histories reported here were also unsuccessful (see Table 2).

Given the large group of successful models, we focus on two models which best represent the extensive range of evolution scenarios generated by our choices of parameters. Moreover, these reference models resemble the model proposed by [33]. The complete temperature, energy, and entropy evolution for models #1 and #15 are respectively shown in the top, middle, and bottom panels of Figure 4.

The evolution of the temperature and the interface radius between the liquid, crystallizing BMO layer and the solid mantle above for each model is shown in Figure 4A and B. Both models share the same imposed cooling history with $Q_{BMO} = 15$ TW and $Q_r = 4$ TW, but have two different dTa/dr values. The initial thickness of the BMO (i.e. interface radius) is defined by the intersection of the melting curve (solid black line) with the adiabat (see Figure 1), and its evolution is controlled by the cooling rate of the layer which is directly dominated by the amount of heat being extracted from the layer, as prescribed by the cooling history curve. As the layer cools over time, the adiabat evolves to lower temperatures (shown as colored dashed lines) intersecting the melting curve at greater depths causing the interface radius to decrease and the liquid layer to shrink towards the CMB. Indeed, the retarding effect dTa/dr has on the evolution of the layer (shown in Figure 3) is evident here as model #1 crystallizes about 1 Gyr sooner than model #15 with the steeper adiabatic gradient.

All the terms in the energy budget outlined in Eq. 8 for both models including an imposed core cooling (yellow curve) term are shown in Figure 4C and D. The most energetic source during the evolution of the BMO layer is the latent heat released as the layer crystallizes, while gravitational rearrangement and secular cooling terms are small. The amount of latent heat released is the largest during the first billion years of evolution as this is when the crystallization rate

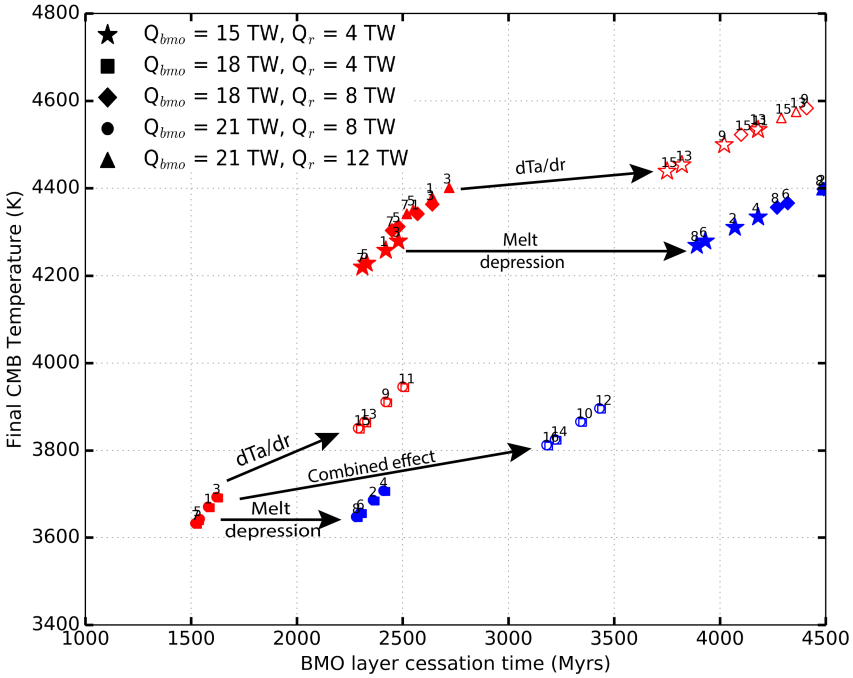

Figure 3: Final CMB temperature. The present-day CMB temperature for all models that successfully crystallized during the age of the Earth are plotted at their corresponding crystallization time. Both adiabatic gradients, $dTa/dr = 1$ (filled markers) and $dTa/dr = 1.2$ (unfilled markers) and both melting point depressions to the melting curve, 700 K (red) and 1100 K (blue) are shown. Schematic arrows show the effect of either parameter in the longevity of the BMO layer for any model run (depicted by the model run numbers) within a given model setup (markers in legend).

is the fastest before being retarded by the imposed melting-point depression on the melting curve. When the layer crystallizes to a thickness of ≈200 - 300 km, the latent heat term becomes comparable to the radiogenic heating and the crystallization rate decreases significantly. Once the layer reaches the CMB, the radiogenic elements are assumed to be trapped in a thin layer atop the CMB, while Q_L and Q_g terms become zero which results in a corresponding jump in core heat flow. The remaining thermal evolution is primarily accommodated by secular cooling of the core according to the prescribed thermal history model (Q_{BMO}) and the assumed heat capacity of the core, resulting in the final T_{CMB} values shown in Figure 3.

The terms in the entropy budget outlined in Eq. 9 for each model are shown in Figure 4E and F, along with the corresponding evolution of the FeO concentration in the liquid layer. As described in the Methods section, the latent heat term is zero for the scenario being considered here. While the gravitational term is small in the energy budget, it is the main contributor of entropy to the system (green curve), with the secular (blue curve) and radiogenic (light blue curve) terms contributing marginally. The cumulative total of these entropy sources is balanced against both thermal conduction (magenta curve) and Ohmic dissipation (yellow curve), which are the entropy sinks in the system.

The entropy of thermal conduction is approximately constant and scales with the choice of thermal conductivity, which is 8 W/m/K for these models. Both models sustain $E_\Phi > 0$ for the first ≈2 billions years, indicating a dynamo would be present in both models over that period of time. However, for BMO dynamos, we consider an additional criteria of whether D_{FeO} is still consistent with the system once it has become highly enriched in Fe. Consequently, we adopt a value of $c^l_{FeO} = 50\, wt\%$ for this threshold, which is shown in the shaded regions. Model #15 (Figure 4F) falls below $E_\Phi = 0$ before this threshold is reached, and for such models as this, we report their dynamo cessation time (starting from t_Φ=0) as the last instance when $E_\Phi > 0$. In contrast, Model #1 (Figure 4E) reaches the threshold while E_Φ is still positive, and for models that encounter this situation, we report the time they reach this threshold as their dynamo cessation.

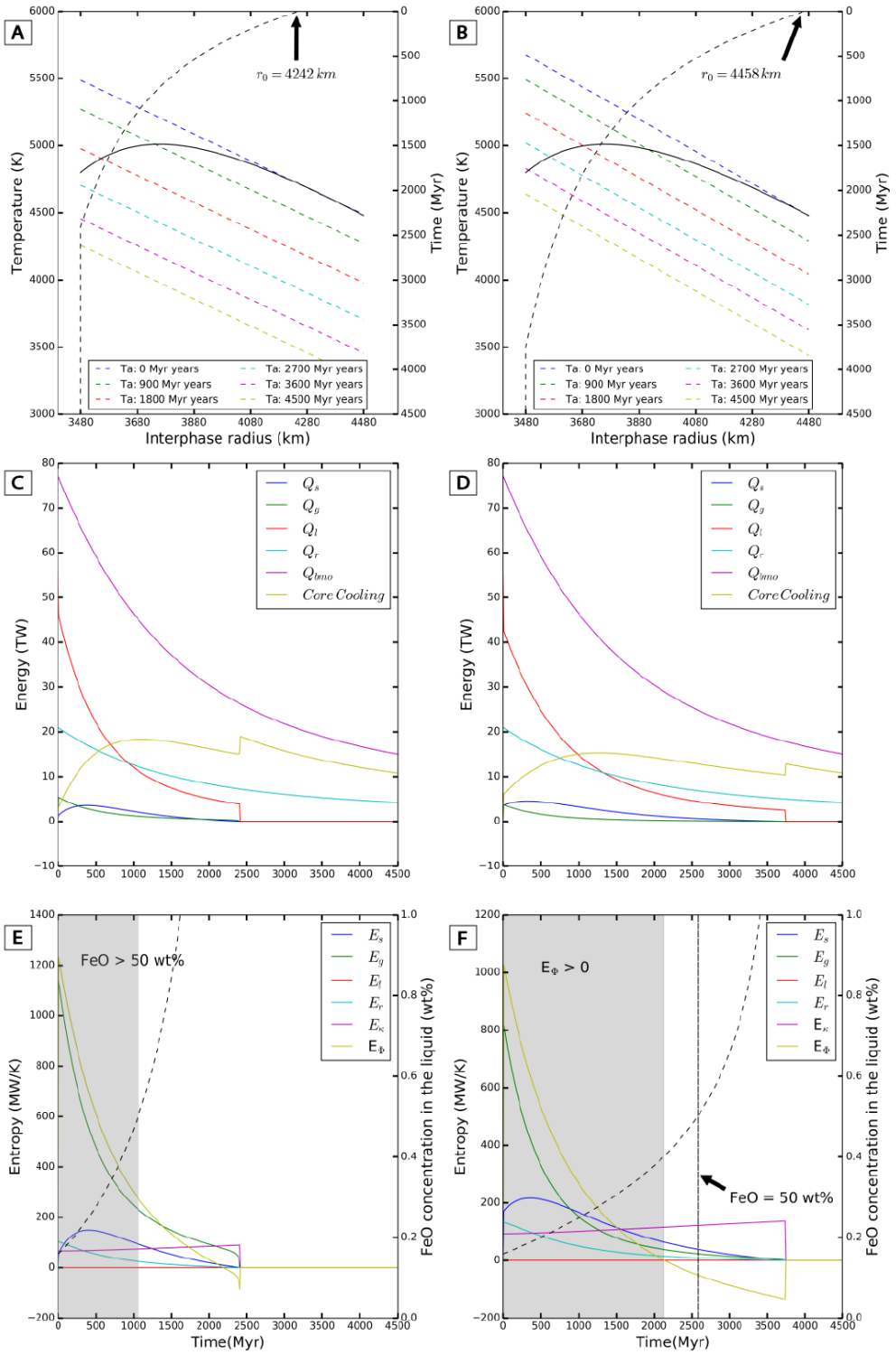

Figure 4: BMO layer evolution. Representative models with $Q_{BMO} = 15$ TW and $Q_r = 4$ TW showing the temperature, energy, and entropy evolution of a 762-km and 978-km thick BMO layer for Models #1 (left column) and Model #15 (right columb), respectively. The evolution of the temperature and thickness of the BMO layer over time controlled by the different adiabatic gradients ($dTa/dr = 1$ K/km for Model #1 and $dTa/dr = 1.2$ K/km for Model #15) are shown on panel A and B, respectively. Each term in the energy budget outlined in Eq. 1 is plotted in C and D for both models over time. The evolution of the associated entropy terms (solid curves) and evolution of the FeO concentration (dashed curve) over time are shown in E and F. Shaded regions show the time interval where $E_\Phi > 0$ while the FeO concentration in the liquid is below 50 wt% (panel E), and last instance when $E_\Phi > 0$ in panel F (i.e. when FeO concentration in run #15 reaches 50%, $E_\Phi < 0$).

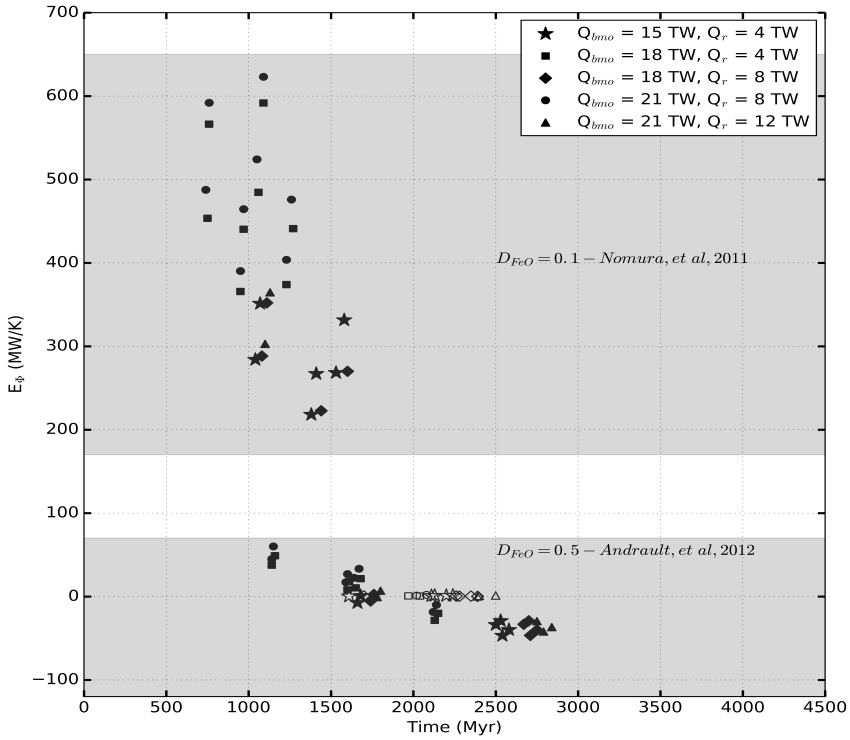

Figure 5: Entropy of Ohmic dissipation over time for all models (at $c^l_{FeO} = 50\,wt\%$) whose BMO layer fully crystallized during the age of the Earth plotted in black (filled). For models with $E_\Phi < 0$ at this cutoff, their entropy value is plotted at the last time when it was positive in black (unfilled). Markers indicate the five difference Q_{BMO}-Q_r scenarios imposed as described in the text. Two distinct clusters, indicated by the shaded regions, capture the influence of the two different partition coefficient values.

We consider this threshold value as a conservative estimate given that E_Φ is well above zero when this point is reached and it would be likely for a dynamo to be operating beyond this time. The partitioning of Fe into the remaining liquid at the solidification front is the mechanism for generating gravitational entropy, which is the dominant term in the entropy budget and controls the magnitude of the Ohmic dissipation. The rate at which the fluid is enriched with Fe, and speed at which the threshold value is reached, is determined by the value of D_{FeO}. Model #1, with $D_{FeO} = 0.1$, results in c^l_{FeO} increasing more rapidly (dashed line in Figure 4E) than measured increases of c^l_{FeO} in Model #15, with $D_{FeO} = 0.5$ (dashed line in Figure 4F). Therefore, the dynamo generated by model #1 (Figure 4E) is roughly 20% more energetic than that of model #15 (Figure 4F).

The amount of entropy available to sustain a dynamo varies among all successful models. Model results for all runs including the available entropy (at $c^l_{FeO} = 50\,wt\%$), their corresponding dynamo and BMO cessation times, and their final CMB temperatures are shown in Table 2. Figure 5 shows the amount of Ohmic dissipation at the time the BMO composition encountered the threshold value of $c^l_{FeO} = 50\,wt\%$ for all models that fully crystallized within the age of the Earth. The two clear populations of models shown in Figure 5 are primarily controlled by the two, end-member values for the partition coefficient of FeO. Models with $D_{FeO} = 0.1$ [43] give rise to long-lived dynamos with lower Ohmic dissipation while those with $D_{FeO} = 0.5$ [44] result in dynamos that are short-lived and larger values of E_Φ. Both scenarios, however, result in models with sufficiently large E_Φ values for the first 1.5 Gyrs -implying an active dynamo during this time.

Combining our results from Figure 3 for how long it takes the BMO layer to fully crystallize and, in each of those models, how long a dynamo would be active from Figure 5, we can see there exists a wide range of scenarios for a BMO dynamo as shown in Figure 6. These scenarios can be summarized in four distinct populations: Short-lived BMO with (1) short-lived, intense dynamo, and (2) long-lived, weaker dynamo; and long-lived BMO with (3) short-lived, intense dynamo, and (4) long-lived, weaker dynamo.

The intensity of the dynamo is regulated by the value of D_{FeO} while the time required for the layer to completely solidify is controlled by both melting-point depression and the choice of adiabatic gradient. Those models with the

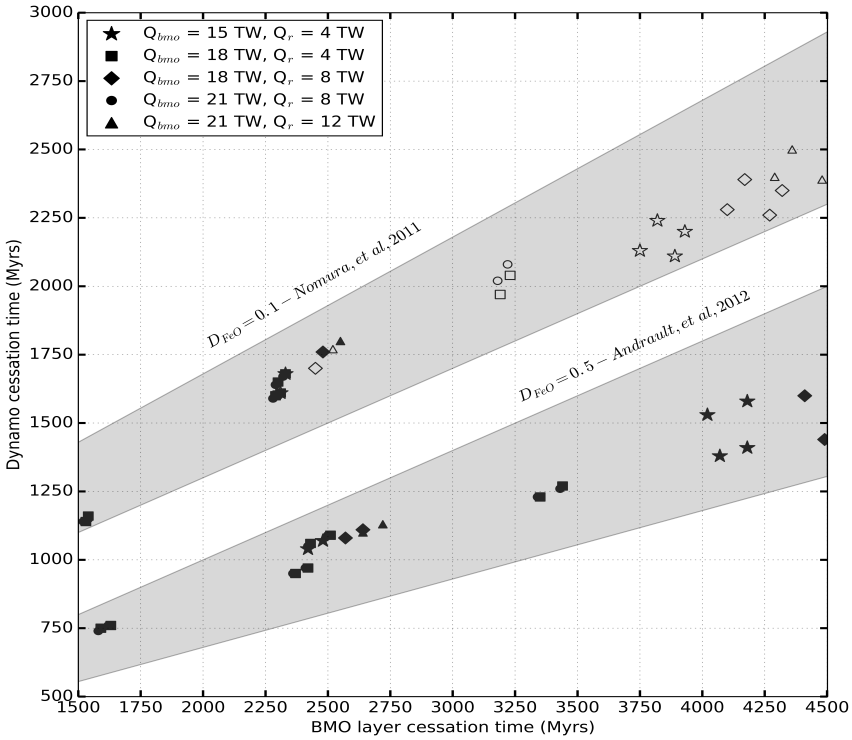

Figure 6: Duration of dynamo activity versus BMO layer crystallization time for all models that fully crystallized. Models with $E_\Phi > 0$ at $c^l_{FeO} = 50\,wt\%$ are plotted in black (filled), while those whose E_Φ value was negative at $c^l_{FeO} = 50\,wt\%$ are plotted in black (unfilled) at the last time E_Φ was above zero. Shaded regions as per Figure 5.

smaller melting-point depression (e.g. $T^0_m = 700$ K) and a partition coefficient $D_{FeO} = 0.1$ result in short-lived BMO layers with roughly 60% more entropy available (at $c^l_{FeO} = 50\,wt\%$) to sustain a dynamo compared to the cases with $D_{FeO} = 0.5$. A smaller D_{FeO} value results in faster Fe enrichment of the liquid layer and correspondingly higher values of entropy generated due to the larger density jump at the interface (e.g. larger E_g term). Indeed, extending the timescale for solidification of the BMO, by imposing a larger melting-point depression, increases the amount of entropy available to sustain magnetic activity for a longer period of time. It is plausible to have models extending the entire shaded area in Figure 6 through a different combination of allowable model parameters and a less conservative cutoff (i.e. $> c^l_{FeO} = 50\,wt\%$).

4 Discussion

The present-day CMB temperature for all successful models shown here (Figure 3) falls within a plausible value (4000±500 K) for the best estimates up to date [49]. The thermal evolution of a BMO layer atop the liquid core over time is heavily dominated by two parameters: the adiabatic gradient in the liquid, and the melting curve for a lower mantle composition; most importantly how depressed this curve becomes at near-CMB pressures and temperatures.

The entropy budget of a BMO-powered dynamo are heavily dominated by the choice in partition coefficient for FeO in the liquid, and, in particular, its evolution as the layer becomes heavily-enriched; such behavior is poorly constrained up to date. We anticipate that D_{FeO} will actually start closer to a value of 0.1 [43] and evolve to larger values as the BMO layer decreases in size, thus we believe our end-member choices for D_{FeO} bracket the expected behavior. Such evolution would in turn result in highly energetic dynamo for the first few hundred million years, similar to Figure 4E, with sustained Ohmic dissipation values beyond 2 Gyrs, resembling the scenario shown in Figure 4F with the higher D_{FeO} value.

Our models successfully show that a crystallizing BMO can be an effective mechanism for generating and sustaining a dynamo throughout early Earth. Most importantly, all models whose BMO layer successfully crystallized during the age of the Earth have sufficient entropy to generate magnetic activity for at least the first 1.5 Gyrs (Figure 5), with some lasting well passed 2 Gyrs. A vast range of parameter combinations other than the choices we made would also lead to

scenarios with enough entropy to generate a dynamo for at least 1.5 Gyrs, conservatively. This makes a BMO-driven dynamo a plausible mechanism for explaining the existence of a magnetic field early on in Earth's history as required by paleomagnetic observations; thus relaxing the need for a global magnetic field to be entirely powered by thermal cooling of the core. Additionally, since exsolution-based mechanisms are also contingent upon the presence of a BMO of some depth, the BMO-powered dynamo is not mutually exclusive with them and the possibility exists for both to operate, either contemporaneously or sequentially.

The time required to fully crystallize a BMO layer as well as the duration of a dynamo that such evolution would produce varies greatly among models (Figure 6). However, it is possible to have some scenarios where a dynamo can be sustained (e.g. $E_\Phi > 0$) for a longer time window given the conservative cutoff employed here, all while also constraining its BMO layer to be fully crystallized at present day and a CMB temperature in agreement with current best estimates. Previous work emphasized that "thermal catastrophe" outcomes were constraints for model evolutions and used this as a basis for determining which combinations of parameters were deemed successful [12, 13, 14], however, by these standards all of our models would be unsuccessful which demonstrates this logic is not sound. Instead, we propose the only constraint that must be satisfied is that the mantle with an initial BMO must completely solidify within the age of the Earth, and if not, this is what we would refer to as unsuccessful model. There is nothing catastrophic or implausible about thermal evolutions that exceed the solidus temperatures for part of their evolution.

5 Conclusion

The evolution of a crystallizing basal magma ocean overlying the liquid core can explain the magnetic evolution of early Earth as most models tested here are energetic enough to sustain a dynamo during this time. Indeed, some of the models sustain dynamos well into the Archaen, though marginally.

The evolution of a basal magma ocean, as modeled here, depends heavily on the material properties of silicates in general and silicate melts in particular. Parameters such as the partitioning coefficient for a molten silicate layer and its evolution as the layer becomes highly enriched in FeO (i.e. $c^l_{FeO} > 50$ wt%), as well as the associated melting-point depression of such a composition at near-CMB pressure and temperature conditions are crucial parameters yet they are poorly constrained to date. The work presented here, while it provides a novel mechanism to generate a dynamo and understand Earth's complex magnetic history, should serve as motivation to better constrain these parameters experimentally.

Moreover, the versatility of this model does not hinge on a specific condition of core cooling; in fact, it can be adapted to complement thermal evolution models involving any thermal conductivity values for the core. More importantly, this model complements previous dynamo mechanism proposed by being able to generate enough power to induce and sustain an early dynamo whose lifespan can be extended by different mechanism (e.g. the Mg exsolution of [16]). A similar computational formulation can be relevant to simulate thermal history schemes in "super-Earth" exoplanets.

References

[1] John A Tarduno, Rory D Cottrell, Michael K Watkeys, Axel Hofmann, Pavel V Doubrovine, Eric E Mamajek, Dunji Liu, David G Sibeck, Levi P Neukirch, and Yoichi Usui. Geodynamo, solar wind, and magnetopause 3.4 to 3.45 billion years ago. *Science*, 327(5970):1238–1240, 2010.

[2] John A Tarduno, Rory D Cottrell, William J Davis, Francis Nimmo, and Richard K Bono. A Hadean to Paleoarchean geodynamo recorded by single zircon crystals. *Science*, 349(6247):521–524, 2015.

[3] Nico de Koker, Gerd Steinle-Neumann, and Vojtěch Vlček. Electrical resistivity and thermal conductivity of liquid Fe alloys at high P and T, and heat flux in Earth's core. *Proceedings of the National Academy of Sciences*, 109(11):4070–4073, 2012.

[4] Monica Pozzo, Chris Davies, David Gubbins, and Dario Alfe. Thermal and electrical conductivity of iron at Earth's core conditions. *Nature*, 485(7398):355, 2012.

[5] Hitoshi Gomi, Kenji Ohta, Kei Hirose, Stephane Labrosse, Razvan Caracas, Matthieu J Verstraete, and John W Hernlund. The high conductivity of iron and thermal evolution of the Earth's core. *Physics of the Earth and Planetary Interiors*, 224:88–103, 2013.

[6] Peter Olson. The new core paradox. *Science*, 342(6157):431–432, 2013.

[7] Christopher J Davies. Cooling history of Earth's core with high thermal conductivity. *Physics of the Earth and Planetary Interiors*, 247:65–79, 2015.

[8] Stéphane Labrosse. Thermal evolution of the core with a high thermal conductivity. *Physics of the Earth and Planetary Interiors*, 247:36–55, 2015.

[9] F Nimmo. Energetics of the core: Ed. G. Schubert. *Treatise on geophysics (second edition). Elsevier, Oxford*, 8:27–55, 2015.

[10] Bruce A Buffett, Herbert E Huppert, John R Lister, and Andrew W Woods. On the thermal evolution of the Earth's core. *Journal of Geophysical Research: Solid Earth*, 101(B4):7989–8006, 1996.

[11] David J Stevenson. Planetary magnetic fields. *Earth and planetary science letters*, 208(1-2):1–11, 2003.

[12] Jun Korenaga. Initiation and evolution of plate tectonics on Earth: theories and observations. *Annual review of earth and planetary sciences*, 41:117–151, 2013.

[13] Jun Korenaga. Urey ratio and the structure and evolution of Earth's mantle. *Reviews of Geophysics*, 46(2), 2008.

[14] P Driscoll and D Bercovici. On the thermal and magnetic histories of Earth and Venus: Influences of melting, radioactivity, and conductivity. *Physics of the Earth and Planetary Interiors*, 236:36–51, 2014.

[15] Joseph G O'Rourke and David J Stevenson. Powering Earth's dynamo with magnesium precipitation from the core. *Nature*, 529(7586):387, 2016.

[16] Joseph G O'Rourke, Jun Korenaga, and David J Stevenson. Thermal evolution of Earth with magnesium precipitation in the core. *Earth and Planetary Science Letters*, 458:263–272, 2017.

[17] James Badro, Julien Siebert, and Francis Nimmo. An early geodynamo driven by exsolution of mantle components from Earth's core. *Nature*, 536(7616):326, 2016.

[18] Kei Hirose, Guillaume Morard, Ryosuke Sinmyo, Koichio Umemoto, John Hernlund, George Helffrich, and Stéphane Labrosse. Crystallization of silicon dioxide and compositional evolution of the Earth's core. *Nature*, 543(7643):99, 2017.

[19] James Badro, Julien Aubert, Kei Hirose, Ryuichi Nomura, Ingrid Blanchard, Stephan Borensztajn, and Julien Siebert. Magnesium Partitioning Between Earth's Mantle and Core and its Potential to Drive an Early Exsolution Geodynamo. *Geophysical Research Letters*, 45(24):13–240, 2018.

[20] Zhixue Du, Colin Jackson, Neil Bennett, Peter Driscoll, Jie Deng, Kanani KM Lee, Eran Greenberg, Vitali B Prakapenka, and Yingwei Fei. Insufficient energy from MgO exsolution to power early geodynamo. *Geophysical Research Letters*, 44(22):11–376, 2017.

[21] Zhixue Du, Asmaa Boujibar, Peter Driscoll, and Yingwei Fei. Experimental constrains on an MgO exsolution-driven geodynamo. *Geophysical Research Letters*, 2019.

[22] Stéphane Labrosse, JW Hernlund, and Nicolas Coltice. A crystallizing dense magma ocean at the base of the Earth's mantle. *Nature*, 450(7171):866, 2007.

[23] Matthieu Laneuville, John Hernlund, Stéphane Labrosse, and Nicholas Guttenberg. Crystallization of a compositionally stratified basal magma ocean. *Physics of the Earth and Planetary Interiors*, 276:86–92, 2018.

[24] Robin M Canup and Erik Asphaug. Origin of the Moon in a giant impact near the end of the Earth's formation. *Nature*, 412(6848):708, 2001.

[25] Matija Ćuk and Sarah T Stewart. Making the Moon from a fast-spinning Earth: a giant impact followed by resonant despinning. *Science*, 338(6110):1047–1052, 2012.

[26] Simon J Lock, Sarah T Stewart, Michail I Petaev, Zoë Leinhardt, Mia T Mace, Stein B Jacobsen, and Matija Cuk. The origin of the Moon within a terrestrial synestia. *Journal of Geophysical Research: Planets*, 123(4):910–951, 2018.

[27] Lars Stixrude, Nico de Koker, Ni Sun, Mainak Mookherjee, and Bijaya B Karki. Thermodynamics of silicate liquids in the deep Earth. *Earth and Planetary Science Letters*, 278(3-4):226–232, 2009.

[28] Nico De Koker and Lars Stixrude. Self-consistent thermodynamic description of silicate liquids, with application to shock melting of MgO periclase and MgSiO3 perovskite. *Geophysical Journal International*, 178(1):162–179, 2009.

[29] C-E Boukaré, Y Ricard, and Guillaume Fiquet. Thermodynamics of the MgO-FeO-SiO2 system up to 140 GPa: Application to the crystallization of Earth's magma ocean. *Journal of Geophysical Research: Solid Earth*, 120(9):6085–6101, 2015.

[30] C-E Boukaré and Y Ricard. Modeling phase separation and phase change for magma ocean solidification dynamics. *Geochemistry, Geophysics, Geosystems*, 18(9):3385–3404, 2017.

[31] Aaron S Wolf and Dan J Bower. An equation of state for high pressure-temperature liquids (RTpress) with application to MgSiO3 melt. *Physics of the Earth and Planetary Interiors*, 278:59–74, 2018.

[32] Razvan Caracas, Kei Hirose, Ryuichi Nomura, and Maxim D Ballmer. Melt–crystal density crossover in a deep magma ocean. *Earth and Planetary Science Letters*, 516:202–211, 2019.

[33] LB Ziegler and DR Stegman. Implications of a long-lived basal magma ocean in generating Earth's ancient magnetic field. *Geochemistry, Geophysics, Geosystems*, 14(11):4735–4742, 2013.

[34] DK Spaulding, RS McWilliams, R Jeanloz, JH Eggert, PM Celliers, DG Hicks, GW Collins, and RF Smith. Evidence for a phase transition in silicate melt at extreme pressure and temperature conditions. *Physical Review Letters*, 108(6):065701, 2012.

[35] R Stewart McWilliams, Dylan K Spaulding, Jon H Eggert, Peter M Celliers, Damien G Hicks, Raymond F Smith, Gilbert W Collins, and Raymond Jeanloz. Phase transformations and metallization of magnesium oxide at high pressure and temperature. *Science*, 338(6112):1330–1333, 2012.

[36] François Soubiran and Burkhard Militzer. Electrical conductivity and magnetic dynamos in magma oceans of Super-Earths. *Nature communications*, 9(1):3883, 2018.

[37] E Holmström, L Stixrude, R Scipioni, and AS Foster. Electronic conductivity of solid and liquid (Mg, Fe) O computed from first principles. *Earth and Planetary Science Letters*, 490:11–19, 2018.

[38] Stephen Stackhouse, Lars Stixrude, and Bijaya B Karki. Thermal conductivity of periclase (MgO) from first principles. *Physical review letters*, 104(20):208501, 2010.

[39] Roberto Scipioni, Lars Stixrude, and Michael P Desjarlais. Electrical conductivity of SiO2 at extreme conditions and planetary dynamos. *Proceedings of the National Academy of Sciences*, 114(34):9009–9013, 2017.

[40] Lars Stixrude. Melting in super-earths. *Philosophical Transactions of the Royal Society A: Mathematical, Physical and Engineering Sciences*, 372(2014):20130076, 2014.

[41] David Gubbins, Dario Alfe, Guy Masters, G David Price, and MJ Gillan. Can the Earth's dynamo run on heat alone? *Geophysical Journal International*, 155(2):609–622, 2003.

[42] David Gubbins, Dario Alfe, Guy Masters, G David Price, and Michael Gillan. Gross thermodynamics of two-component core convection. *Geophysical Journal International*, 157(3):1407–1414, 2004.

[43] Ryuichi Nomura, Haruka Ozawa, Shigehiko Tateno, Kei Hirose, John Hernlund, Shunsuke Muto, Hirofumi Ishii, and Nozomu Hiraoka. Spin crossover and iron-rich silicate melt in the Earth's deep mantle. *Nature*, 473(7346):199, 2011.

[44] Denis Andrault, Sylvain Petitgirard, Giacomo Lo Nigro, Jean-Luc Devidal, Giulia Veronesi, Gaston Garbarino, and Mohamed Mezouar. Solid–liquid iron partitioning in Earth's deep mantle. *Nature*, 487(7407):354, 2012.

[45] G Fiquet, AL Auzende, J Siebert, A Corgne, H Bureau, H Ozawa, and G Garbarino. Melting of peridotite to 140 gigapascals. *Science*, 329(5998):1516–1518, 2010.

[46] Adam M Dziewonski and Don L Anderson. Preliminary reference Earth model. *Physics of the earth and planetary interiors*, 25(4):297–356, 1981.

[47] William F McDonough and S-S Sun. The composition of the Earth. *Chemical Geology*, 120(3-4):223–253, 1995.

[48] Stéphane Labrosse. Thermal and magnetic evolution of the Earth's core. *Physics of the Earth and Planetary Interiors*, 140(1-3):127–143, 2003.

[49] S Anzellini, A Dewaele, M Mezouar, P Loubeyre, and G Morard. Melting of iron at Earth's inner core boundary based on fast X-ray diffraction. *Science*, 340(6131):464–466, 2013.